Machine-Learning Optimization of Multiple Measurement Parameters Nonlinearly Affecting the Signal Quality

AUTHOR(S):

Fujisaku, Takahiro; So, Frederick Tze Kit; Igarashi, Ryuji; Shirakawa, Masahiro

CITATION:

Fujisaku, Takahiro ...[et al]. Machine-Learning Optimization of Multiple Measurement Parameters Nonlinearly Affecting the Signal Quality. ACS Measurement Science Au 2021, 1(1): 20-26

ISSUE DATE:

2021-08-18

URL:

http://hdl.handle.net/2433/277797

ACS MEASUREMENT SCIENCE Au
AN OPEN ACCESS JOURNAL OF THE AMERICAN CHEMICAL SOCIETY

pubs.acs.org/measureau Article

Machine-Learning Optimization of Multiple Measurement Parameters Nonlinearly Affecting the Signal Quality

Takahiro Fujisaku,[#] Frederick Tze Kit So,[#] Ryuji Igarashi,*[,#] and Masahiro Shirakawa*

Cite This: *ACS Meas. Au* 2021, 1, 20–26 Read Online

ACCESS | Metrics & More | Article Recommendations | Supporting Information

ABSTRACT: Determination of optimal measurement parameters is essential for measurement experiments. They can be manually optimized if the linear correlation between them and the corresponding signal quality is known or easily determinable. However, in practice, this correlation is often nonlinear and not known a priori; hence, complicated trial and error procedures are employed for finding optimal parameters while avoiding local optima. In this work, we propose a novel approach based on machine learning for optimizing multiple measurement parameters, which nonlinearly influence the signal quality. Optically detected magnetic resonance measurements of nitrogen-vacancy centers in fluorescent nanodiamonds were used as a proof-of-concept system. We constructed a suitable dataset of optically detected magnetic resonance spectra for predicting the optimal laser and microwave powers that deliver the highest contrast and signal-to-noise ratio values by means of linear regression, neural networks, and random forests. The model developed by the considered neural network turned out to have a coefficient of determination significantly higher than that of the other methods. The proposed method thus provided a novel approach for the rapid setting of measurement parameters that influence the signal quality in a nonlinear way, opening a gate for fields like nuclear magnetic resonance, electron paramagnetic resonance, and fluorescence microscopy to benefit from it.

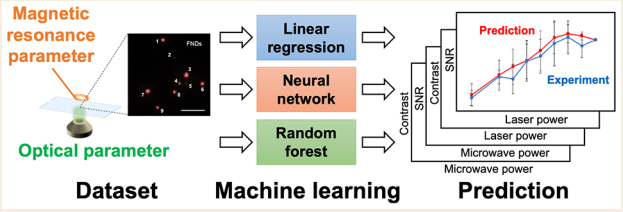

KEYWORDS: *Optically detected magnetic resonance, signal-to-noise ratio, nitrogen-vacancy centers, fluorescence microscopy, neural networks, signal processing*

INTRODUCTION

Advances in biological measurement techniques, such as fluorescence microscopy and magnetic resonance, made it possible to semiautomatically obtain a variety of information about various biological samples, including biomolecules and cells.[1−3] However, in order to increase the quality of the recorded signals, it is recommended to take the measurement parameter close to its optimal value. In order to achieve this, many sophisticated measurement user interfaces provide automatic measurement parameter optimization capabilities. For instance, in confocal fluorescence imaging, various parameters including exposure time, excitation power, and pinhole size are optimized in order to obtain the highest possible fluorescence intensity and resolution while minimizing photobleaching. In nuclear magnetic resonance (NMR) measurement, the measurement sensitivity and line width vary significantly depending on the quality of tuning, matching, and shimming.[4]

In many cases, the automatic optimization of multiple measurement parameters is based on linear optimization by exploiting the linear correlation between measurement parameters and the quality of the signals achievable under mild conditions. However, in order to automatically optimize the measurement parameters for achieving the best quality of the signals by means of linear optimization, while avoiding local optima, the measurement parameters need to be adequately limited a priori or the optimal initial value has to be known. Actually, even in the traditional automatic optimization of NMR tuning matching, choosing an initial value too far away from the optimum can make the procedure stuck in an unwanted useless local optimum. Therefore, it is highly desirable that local optima are avoided and measurement parameter values close to the global optimum are found, whenever necessary, even by manually solving a multivariate constrained nonlinear optimization problem. In semiautomated measurements, this issue can turn out to be quite costly in terms of time and consumed resources. On the other hand, prediction of interaction between multiple nonlinear effects is generally difficult due to crosstalk among them.[5]

Machine learning is suitable for modeling nonlinear parameters[6−8] by facilitating the optimization of measurement parameters that have a nonlinear effect on the quality of the obtained signals. With this study, we contribute to demon-

Received: May 14, 2021
Published: July 1, 2021

https://doi.org/10.1021/acsmeasuresciau.1c00009
ACS Meas. Au 2021, 1, 20–26

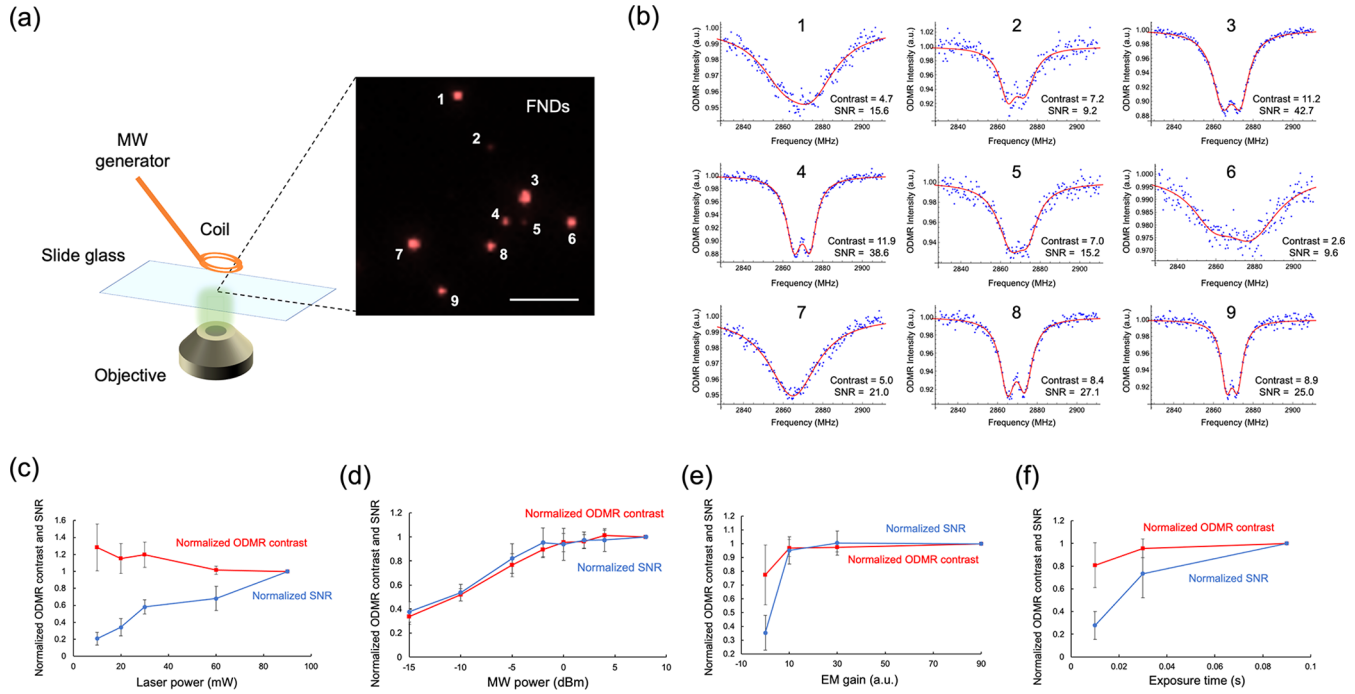

Figure 1. Creation of datasets for training and testing the machine-learning model for predicting ODMR contrast and SNR under different conditions. (a) Setup for wide-field fluorescence imaging of FNDs to obtain multiple ODMR spectra at once. FNDs were attached to a coverslip by hydrophobic interaction and then irradiated with MW by a copper wire coil. The scale bar represents 5 μm. The inset is a typical fluorescence image of FNDs. The wide variety of fluorescence intensity is caused by the difference in particle size, which correlates with the number of NV centers. (b) Example of ODMR spectra where the laser power was 30 mW, EM gain was 20, MW power was 0 dBm, and the exposure time was 0.01 s. ODMR spectra were fitted by two Lorentzian functions to calculate their contrasts and SNRs. Note that the ODMR contrast and SNR do not depend only on the fluorescence signal intensity. (c–f) Average changes of ODMR contrasts and SNRs plotted against the ODMR parameters of (c) laser power, (d) MW power, (e) EM gain, and (f) exposure time. Each ODMR contrast and SNR were normalized by that at a (c) laser power of 90 mW, (d) MW power of 6 dBm, (e) EM gain of 90, and (f) exposure time of 0.09 s. Error bars represent the standard deviation from nine FNDs presented in (a).

strating the efficacy of machine-learning methods in optimizing multiple measurement parameters.

To perform the necessary proof-of-concept experiments, we use a system of optically detected magnetic resonance (ODMR) of nitrogen-vacancy centers (NVCs) contained by fluorescent nanodiamonds (FNDs), which encapsulates aspects of both fluorescence microscopy and magnetic resonance. NVCs have recently attracted attention as highly sensitive and ultrasmall quantum sensors for thermometry[9−13] and magnetometry,[14−16] and their applications include cell nanothermometry with an accuracy of ±1 K as well as the detection of extremely weak magnetic signals from neuron signaling.[9,17−19] Quantum sensing using NVCs is based on ODMR, which reports the quantum state through optical methods, enabling the quantification of physical quantities on which the quantum state of NVCs depends.[20−23] In ODMR-based quantification of physical quantities, the contrast and signal-to-noise ratio (SNR) of the ODMR spectrum directly affect the process sensitivity; thus, it is important to set the measurement parameters optimally with respect to both contrast and SNR. However, in conventional protocols, it is necessary to measure ODMR spectra and adjust the measurement parameters with ambiguous guidelines, which takes a long time and may damage the samples or produce low sensitivity. The main difficulty in creating guidelines comes from the fact that multiple parameters, such as NVC concentration, electron-multiplying (EM) gain, laser power, and microwave (MW) power, affect the resulting contrast and SNR in a nonlinear way.[24−26] In particular, the contrast decreasing could be caused by the charge exchanges of NVCs and nitrogen impurity at high optical excitation rates.[27] Moreover, the ODMR intensity I depends on the MW excitation power P, obeying the equation $I = I_{max}/(1 + P_{max}/P)$ phenomenologically, where P_{max} is the −3 dB saturation level.[28] Therefore, ODMR contrast should be optimum below saturation levels by adjusting the laser power and MW. In this paper, we demonstrate the feasibility of machine-learning optimization of the excitation laser and magnetic resonance MW powers, which have nonlinear effects on both ODMR contrast and SNR. We present a machine-learning method for constructing a model for predicting the contrast and SNR only from the input parameters. To this end, we first built a large dataset of ODMR spectra using wide-field microscopy. By introducing a large and homogeneous laser and MW radiation to a large number of (multiple types of) FND particles, a database of ODMR spectra under various conditions was obtained. This was then processed via machine learning by employing different methods (i.e., linear regression, neural networks, and random forests) to predict the resulting ODMR contrast and SNR of the spectrum from only the input experimental conditions. Finally, the prediction model was evaluated in terms of accuracy by random sampling, exhibiting high accuracy and practical usefulness.

https://doi.org/10.1021/acsmeasuresciau.1c00009
ACS Meas. Au 2021, 1, 20−26

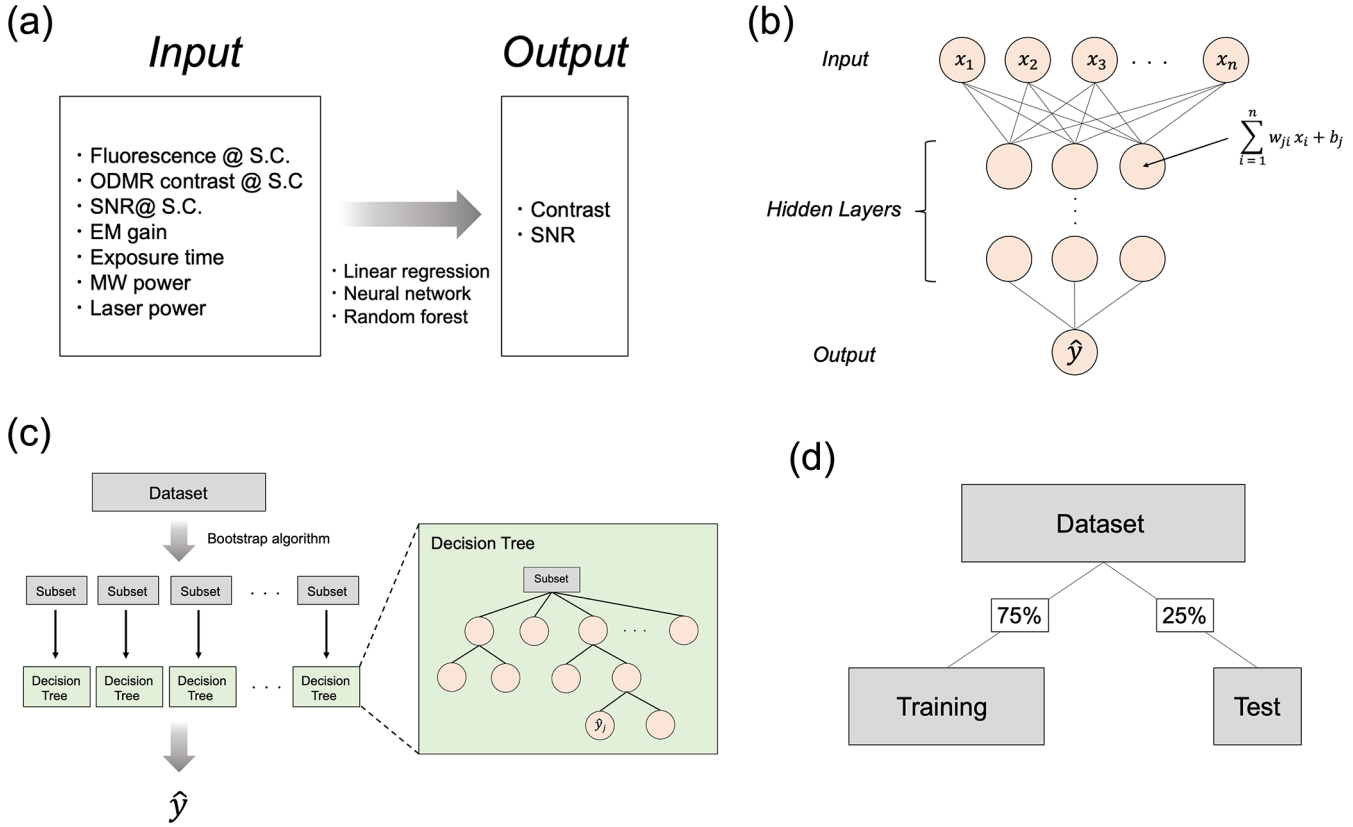

Figure 2. Machine-learning method to predict optically detected magnetic resonance contrast and signal-to-noise ratio. (a) Predictor functions were trained and tested using a dataset containing the displayed inputs and outputs. S.C. represents the standard condition in which the laser power was 30 mW, EM gain was 0, MW power was 0 dBm, and exposure time was 0.01 s. Three widely used machine-learning methods (i.e., linear regression, neural network, and random forest) were employed. (b) Principle of neural network to predict output of $\hat{\mathbf{y}}$ from the input of future parameters of x_n. Weights of w_{ji} were multiplied by each value of a node in a layer, and bias of b_j was added, and these were propagated to the next nodes. These values were normalized using an activation function. The neural network was trained by adjusting w and b to minimize the loss function using gradient descent. (c) Principle of random forest. The training dataset was split into subsets using a bootstrap algorithm, from which decision trees were trained and created. The mean value of decision tree predictions produced $\hat{\mathbf{y}}$. (d) Dataset processing method to train predictor functions. Among the dataset, 75% was randomly selected to train the predictor function, whereas the remaining 25% was used for evaluation.

EXPERIMENTAL SECTION

Preparation of Fluorescent Nanodiamonds

We followed the FND treatment protocol previously reported.[29] Nanodiamond powder (Element Six, Micron+ MDA 0−0.10 μm) was electron-irradiated (2 MeV, 1.0 × 10^{18} e^-/cm^2) and thermally annealed at 800 °C for 2 h under vacuum. The residue was oxidized at 550 °C for 2 h. Then the residue was heat-treated with a mixture of H_2SO_4/HNO_3 (9:1 v/v) at 70 °C for 3 days, followed by 0.1 M NaOH at 90 °C for 2 h and 0.1 M HCl at 90 °C for 2 h. The residue was washed with Milli-Q to produce surface-treated FNDs. The nanodiamonds were the same lot used in the previously reported study, containing 40 negatively charged NVCs per particle on average.[29]

Wide-Field Microscopy

The FNDs were dispersed in Milli-Q to reach 1 mg/mL. Twenty microliters of this solution was placed on a 24 × 60 micro coverslip (Matsunami, thickness no. 1). After 10 min, the solution was washed with Milli-Q. We used an EM charge-coupled device camera (Andor iXon DU897, Andor Technology), green solid-state laser (Coherent, 532 nm; Sapphire 532 LP), and oil immersion 60× objective (Nicon, CFI Apochromat TIRF 60×/1.49). The emitted fluorescence was passed through a dichroic mirror centered at 575 nm and a 650 nm long-wave pass filter. The MW was generated by the MXG analog signal generator (Key Sight, N5181B). The output of laser power density and MW power was monitored using a UVVIS quantum power sensor (Coherent, 1168337) and RF power meter (Agilent, V3500A) (Figure S2). All ODMR spectra had 201 data points and were accumulated 20 times. The accumulation time was 84 s, and the exposure time was 0.01 s.

Machine Learning

Data formatting and training of the predictor function were performed using Wolfram Mathematica (version 12.0.0.0). The ODMR spectra obtained by wide-field microscopy were transformed into the inputs and outputs presented in Figure 2a. Predictor functions were generated using the built-in "Predict" function in Mathematica by specifying "LinearRegression", "NeuralNetwork", or "RandomForest" in "Method". "PerformanceGoal" was set to "Quality" so that the prediction accuracy was maximized.

RESULTS AND DISCUSSION

A wide-field ODMR microscope capable of simultaneous measurements on multiple nanodiamonds was built in order to procure a database of ODMR spectra (more precisely ODMR contrast and SNR values) captured under different conditions that were necessary for training and testing the prediction model. First, a beam expander and copper-coil-based MW irradiation were set up to record ODMR spectra under the widest possible field of vision (Figure 1a). The resulting ODMR spectra were afterward fitted with two Lorentzian functions, and the decrease at the minimum value from the base line of the corresponding function was defined in each

https://doi.org/10.1021/acsmeasuresciau.1c00009
ACS Meas. Au 2021, 1, 20−26

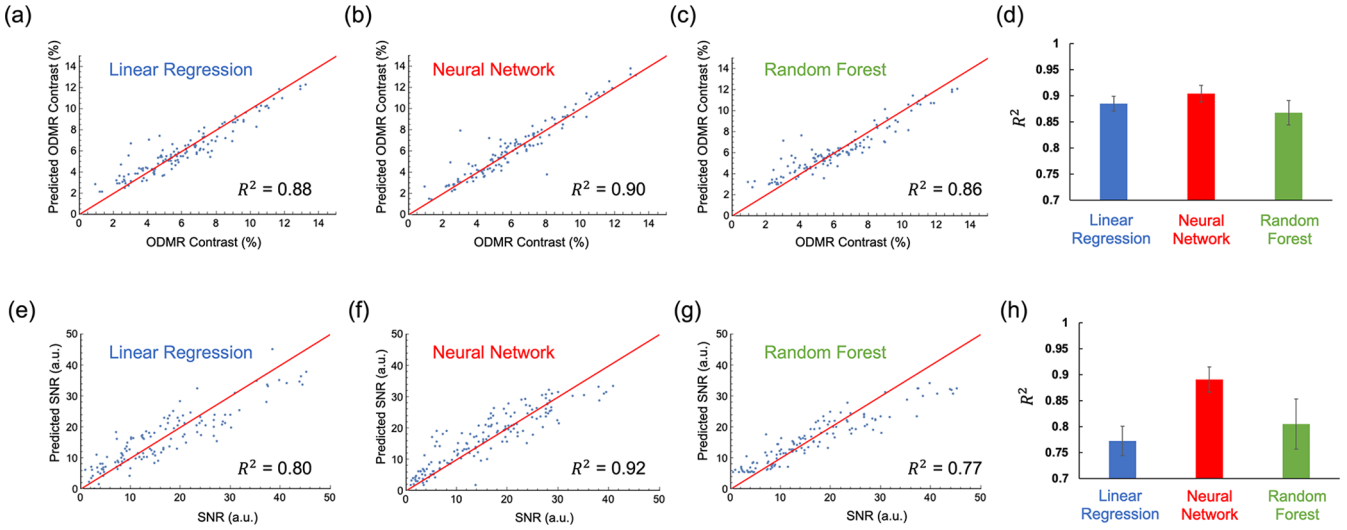

Figure 3. Evaluation of predictor functions. (a–c) Plots of predicted ODMR contrast against ODMR contrast measured using a (a) linear regression, (b) neural network, and (c) random forest. The coefficient of determination R^2 was calculated to quantify how well the outcomes were predicted. Red lines represent the case of $R^2 = 1$. (d) Bar chart of average R^2 in the prediction of ODMR contrasts with each method. The error bar represents the standard deviation of seven experiments. In each experiment, subsets for training and testing were shuffled randomly. (e–g) Plots of predicted SNRs against values measured by a (e) linear regression, (f) neural network, and (g) random forest. (h) Bar chart of average R^2 in the prediction of SNRs with each method.

case as the ODMR contrast. In addition, each ODMR contrast value was divided by the average absolute fit residual, the resulting value being defined as the corresponding SNR (Figure 1b).

To investigate the effect of the ODMR parameters on the contrast and SNR, we measured ODMR spectra under various conditions using the aforementioned setup. When the laser power changed, the results revealed an inverse relationship between contrast and SNR, namely, the lower the contrast, the higher the SNR (Figure 1c). Furthermore, the procedure also revealed that, under relatively low MW power conditions, both contrast and SNR increased, while saturation occurred over 0 dBm (Figure 1d). Upon increasing the EM gain, a significant increase in contrast and SNR in the low photon count condition was observed (Figure 1e), while in the stationary FND experiments, the exposure time tended to have a positive effect on both contrast and SNR, unlike in the case of moving FNDs (Figure 1f).

As illustrated in Figure 1c–f, each measurement parameter had a nonlinear effect on both contrast and SNR taken individually. On the other hand, all of these parameters had a nonlinear effect on each other, too; hence, it was extremely difficult to consider them all manually. We attempted to determine these parameters via machine learning with a large number of ODMR spectra to predict the resulting ODMR contrast and SNR only from input parameters. Actual data (901 ODMR spectra) were collected and loaded into the following machine-learning algorithms: linear regression, neural network, and random forest, in order to predict the ODMR contrast and SNR values by using the input parameters illustrated in Figure 2a. In linear regression, for a vector $X = (x_1, x_2, x_3,..., x_n)$ with n features, the predicted y value was generated by the following formula, where θ_i $(i = 1,..., n)$ and b are the weight and bias and were determined to minimize the difference between the predicted value of $\hat{y}$ and the value of y using a loss function:

$$\hat{y} = \sum_{i=1}^{n} \theta_i x_i + b$$

For the neural network, the predicted value y was generated using nodes arranged in layers (Figure 2b). The weight was multiplied by each value stored in the node of the previous layer, and the bias was added to the sum, which was normalized by an activation function and stored in each node. The predicted value was generated by propagating this process from the input layer to the output layer. The values of w_{ij} and b_j were afterward determined in order to minimize the loss function.

Meanwhile, in the random forest method, the database was divided into random subsets using a bootstrap algorithm (Figure 2c) and subsequently used to generate and train multiple decision trees. These were constructed using the classification and regression tree algorithm. The final output of the random forest was obtained by taking the mean value of the decision tree predictions. For each individual method for generating the predictor model, 75% of the aforementioned dataset was used for training, while the remaining data were used for evaluating the final model (Figure 2d).

To evaluate the accuracy of the prediction function, a part of the database was used for testing it. The coefficient of determination was used to verify the accuracy of the prediction as follows:

$$R^2 = 1 - \frac{\sum_{i=1}^{N} (y_i - \hat{y}_i)^2}{\sum_{j=1}^{N} (y_j - \bar{y})^2}$$

$$\bar{y} = \frac{1}{n} \sum_{i=1}^{N} y_i$$

where N is the total number of samples, y is the observed value, $\bar{y}$ is the total average of y, and $\hat{y}$ is the predicted value.

The experimental ODMR contrast and ODMR contrast predicted by each method were plotted, and the coefficient of

https://doi.org/10.1021/acsmeasuresciau.1c00009
ACS Meas. Au 2021, 1, 20–26

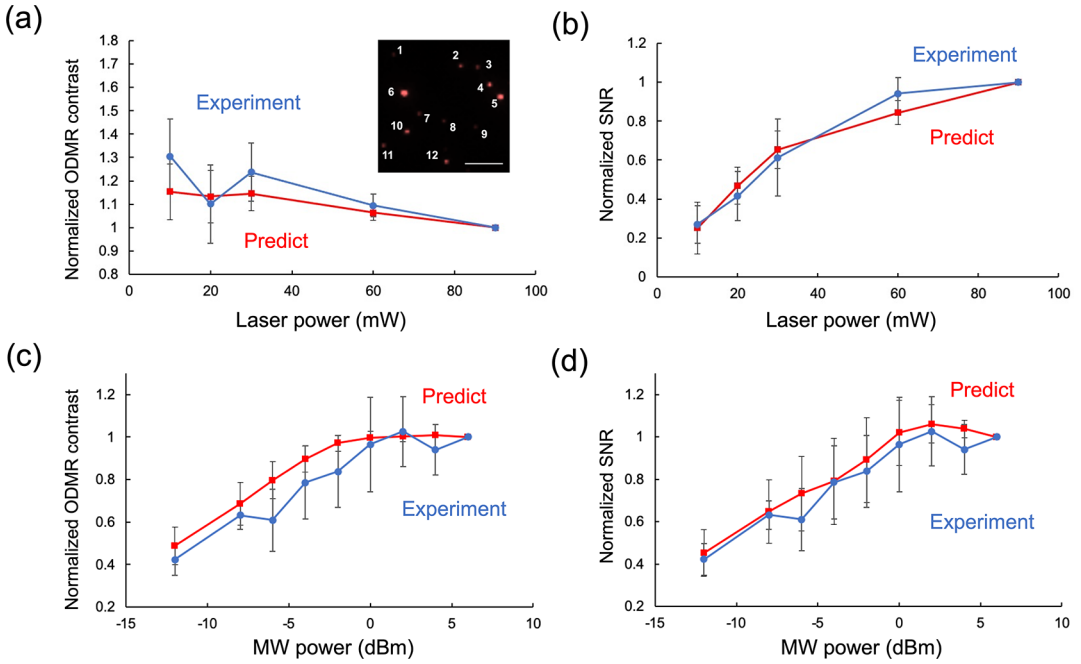

Figure 4. Prediction of ODMR contrast and SNR of unknown FNDs for the optimization of laser power and MW power. Average changes of (a) ODMR contrasts and (b) SNRs are plotted against laser power. Each ODMR contrast and SNR were normalized by that at a laser power of 90 mW. (c) ODMR contrasts and (d) SNRs are plotted against MW power. Each ODMR contrast and SNR were normalized by that at an MW power of 6 dBm. Error bars represent the standard deviation from 12 FNDs illustrated in the inset in (a). The scale bar represents 5 μm. The red lines were obtained from the predictor function based on the neural network, while the blue lines were obtained from experimental results.

determination was calculated in each case[30] (Figure 3a–c). Furthermore, the training and test data were randomly shuffled, and the coefficient of determination was then repeatedly calculated seven times to obtain the mean and standard deviation. The coefficients of determination for linear regression, neural network, and random forest were 0.88 ± 0.01, 0.90 ± 0.02, and 0.87 ± 0.02, respectively (Figure 3d). Using the same method, the SNRs were predicted to have a coefficient of determination of 0.77 ± 0.03, 0.89 ± 0.02, and 0.81 ± 0.05, respectively (Figure 3e–h). These results demonstrate that each model had a significant coefficient of determination, indicating that machine learning was indeed effective in predicting ODMR contrast and SNR through multivariable inputs. It is worth noting that the model developed by the neural network method had a significantly higher coefficient of determination than the other methods, indicating that it was the most effective in predicting ODMR contrast and SNR.

Finally, we worked on optimizing the MW and laser power in the considered ODMR setup using the trained neural network. In practice, high MW and laser power are often problematic, as they produce a significant amount of heat that can induce measurement noise or damage to samples. To this end, we investigated the ODMR contrast and SNR of FNDs that were not present in the training dataset. The ODMR spectra of these FNDs were thus measured by wide-field microscopy under various conditions of laser power and MW power in order to create the corresponding ground-truth dataset. Subsequently, ODMR contrast and SNR were predicted and plotted using the predictor model (Figure 4). The resulting prediction of the ODMR contrast with respect to laser power was determined via experiments, while the trade-off relationship between ODMR contrast and SNR (i.e., ODMR contrast decreased as the SNR increased) was verified as the laser power increased, where the average absolute values of the residuals from the measured values were 6.1 and 4.1%, respectively (Figure 4a,b). Furthermore, in the prediction of MW power, the predictor model estimated that ODMR contrast and SNR would improve due to the increase in MW power; however, they eventually saturate near 0 dBm. The average absolute values of the residuals from the measured values were 7.5 and 4.6%, respectively (Figure 4c,d). Moreover, under untrained conditions, the neural network predicted ODMR contrasts and SNR at high accuracy of R^2 = 0.65 and 0.80, respectively (Figure S1). Altogether, we have thus demonstrated that the trained predictor model based on a neural network is capable of accurately estimating ODMR contrast and SNR only from the input conditions.

Our proposed method can be useful in various conditions. For instance, in dynamic system experiments, the three-dimensional freedom of FNDs is very intricate,[16] and the longer exposure time will reduce the ODMR contrast and SNR due to the fluctuation in focus and fluorescence intensities. In addition, the proposed method can facilitate the high-speed setting of appropriate ODMR measurement parameters. In unstable biological experiments, where intracellular activities often occur in a short period of time, appropriate and high-speed optimization of ODMR parameters, such as laser and MW power, is crucial.[16,19] Moreover, the smallest FNDs, such as detonation nanodiamonds, are highly subject to photobleaching due to the short distance between the NVCs and the surface, and high-speed optimization algorithms are required.[31]

CONCLUSION

In conclusion, we proposed a novel approach based on machine learning for optimizing multiple measurement parameters which nonlinearly influence the quality of the received signals. Three machine-learning algorithms (linear

https://doi.org/10.1021/acsmeasuresciau.1c00009
ACS Meas. Au 2021, 1, 20–26

regression, neural networks, and random forests) were successfully employed for rapidly predicting the optimal laser and MW powers that deliver the highest contrast and signal-to-noise ratio values in optically detected magnetic resonance measurements of nitrogen-vacancy centers in fluorescent nanodiamonds. Our proposed method, which enables the high-speed setting of measurement parameters under intricate situations, can provide the lowest adverse effect on the measurement and highest sensitivity of quantum sensing using NVCs, opening thus a new gate for rapid setting of measurement parameters which influence signal quality in a nonlinear manner. Hence, not only ODMR measurement but also fields such as NMR, electron paramagnetic resonance, and fluorescence microscopy would benefit from it.

■ ASSOCIATED CONTENT

Supporting Information

The Supporting Information is available free of charge at https://pubs.acs.org/doi/10.1021/acsmeasuresciau.1c00009.

Evaluation of predictor functions with the dataset containing future parameters not used in training; measurements of the outputs of laser power densities and microwave power against the inputs (error bar represents standard deviation) (PDF)

■ AUTHOR INFORMATION

Corresponding Authors

Masahiro Shirakawa − *Institute for Quantum Life Science, National Institutes for Quantum and Radiological Science and Technology, Inage-ku, Chiba 263-8555, Japan; Department of Molecular Engineering, Graduate School of Engineering, Kyoto University, Nishikyo-Ku, Kyoto 615-8510, Japan*; Email: shirakawa@moleng.kyoto-u.ac.jp

Ryuji Igarashi − *Institute for Quantum Life Science, National Institutes for Quantum and Radiological Science and Technology, Inage-ku, Chiba 263-8555, Japan; National Institute for Radiological Sciences, National Institute for Quantum and Radiological Science and Technology, Inage-ku, Chiba 263-8555, Japan; JST, PRESTO, Kawaguchi, Saitama 332-0012, Japan;* orcid.org/0000-0003-4415-9702; Email: igarashi.ryuji@qst.go.jp

Authors

Takahiro Fujisaku − *Institute for Quantum Life Science, National Institutes for Quantum and Radiological Science and Technology, Inage-ku, Chiba 263-8555, Japan; Department of Molecular Engineering, Graduate School of Engineering, Kyoto University, Nishikyo-Ku, Kyoto 615-8510, Japan*

Frederick Tze Kit So − *Institute for Quantum Life Science, National Institutes for Quantum and Radiological Science and Technology, Inage-ku, Chiba 263-8555, Japan; Institute for Chemical Research, Kyoto University, Gokasho, Uji, Kyoto 611-0011, Japan*

Complete contact information is available at: https://pubs.acs.org/10.1021/acsmeasuresciau.1c00009

Author Contributions

#T.F., F.T.-K.S., and R.I. contributed equally. T.F. performed all of the measurements. T.F. performed all of the analyses with F.T.-K.S. F.T.K.S. prepared the fluorescent nanodiamond samples with T.F. R.I. constructed the measurement setup. The work was supervised by R.I. and M.S. The manuscript was written through contributions of all authors. All authors have given approval to the final version of the manuscript.

Notes

The authors declare no competing financial interest.

■ ACKNOWLEDGMENTS

This research was funded by a Grant-in-Aid for JSPS Fellows (JSPS KAKENHI Grant No. JP19J12787), a Grant-in-Aid for Scientific Research on Innovative Areas "New measurement techniques for visualizing live protein molecules at work" (JSPS KAKENHI Grant No. JP26119004) and Challenging Research (JSPS KAKENHI Grant No. JP18K19297), JSPS KAKENHI Grant Nos. JP20H02587, JP20H00453, the Japan Science and Technology Agency under Precursory Research for Embryonic Science and Technology (PRESTO, Grant Nos. JPMJPR14F1 and JPMJPR18G1), MEXT Quantum Leap Flagship Program (MEXT Q-LEAP, Grant No. JPMXS0120330644, JPMXS0118067395), CAO Public/Private R&D Investment Strategic Expansion PrograM (CAO PRISM), and AMED (Grant No. JP21zf0127004).

■ REFERENCES

(1) Winkler, T.; Kettling, U.; Koltermann, A.; Eigen, M. Confocal Fluorescence Coincidence Analysis: An Approach to Ultra High-Throughput Screening. *Proc. Natl. Acad. Sci. U. S. A.* **1999**, *96* (4), 1375−1378.

(2) Dalvit, C.; Fagerness, P. E.; Hadden, D. T. A.; Sarver, R. W.; Stockman, B. J. Fluorine-NMR Experiments for High-Throughput Screening: Theoretical Aspects, Practical Considerations, and Range of Applicability. *J. Am. Chem. Soc.* **2003**, *125* (25), 7696−7703.

(3) Conrad, C.; Wünsche, A.; Tan, T. H.; Bulkescher, J.; Sieckmann, F.; Verissimo, F.; Edelstein, A.; Walter, T.; Liebel, U.; Pepperkok, R.; Ellenberg, J. Micropilot: Automation of Fluorescence Microscopy−Based Imaging for Systems Biology. *Nat. Methods* **2011**, *8* (3), 246−249.

(4) Prammer, M. G.; Haselgrove, J. C.; Shinnar, M.; Leigh, J. S. A New Approach to Automatic Shimming. *J. Magn. Reson. (1969-1992)* **1988**, *77* (1), 40−52.

(5) Fan, Q.; Zhou, G.; Gui, T.; Lu, C.; Lau, A. P. T. Advancing Theoretical Understanding and Practical Performance of Signal Processing for Nonlinear Optical Communications through Machine Learning. *Nat. Commun.* **2020**, *11* (1), 3694.

(6) Weng, S. F.; Reps, J.; Kai, J.; Garibaldi, J. M.; Qureshi, N. Can Machine-Learning Improve Cardiovascular Risk Prediction Using Routine Clinical Data? *PLoS One* **2017**, *12* (4), e0174944.

(7) Bunker, R. P.; Thabtah, F. A Machine Learning Framework for Sport Result Prediction. *Applied Computing and Informatics* **2019**, *15* (1), 27−33.

(8) Chen, J. H.; Asch, S. M. Machine Learning and Prediction in Medicine — Beyond the Peak of Inflated Expectations. *N. Engl. J. Med.* **2017**, *376* (26), 2507−2509.

(9) Kucsko, G.; Maurer, P. C.; Yao, N. Y.; Kubo, M.; Noh, H. J.; Lo, P. K.; Park, H.; Lukin, M. D. Nanometre-Scale Thermometry in a Living Cell. *Nature* **2013**, *500* (7460), 54−58.

(10) Acosta, V. M.; Bauch, E.; Ledbetter, M. P.; Waxman, A.; Bouchard, L.-S.; Budker, D. Temperature Dependence of the Nitrogen-Vacancy Magnetic Resonance in Diamond. *Phys. Rev. Lett.* **2010**, *104* (7), 070801.

(11) Fujiwara, M.; Sun, S.; Dohms, A.; Nishimura, Y.; Suto, K.; Takezawa, Y.; Oshimi, K.; Zhao, L.; Sadzak, N.; Umehara, Y.; Teki, Y.; Komatsu, N.; Benson, O.; Shikano, Y.; Kage-Nakadai, E. Real-Time Nanodiamond Thermometry Probing in Vivo Thermogenic Responses. *Science Advances* **2020**, *6* (37), eaba9636.

(12) Sotoma, S.; Zhong, C.; Kah, J. C. Y.; Yamashita, H.; Plakhotnik, T.; Harada, Y.; Suzuki, M. In Situ Measurements of Intracellular Thermal Conductivity Using Heater-Thermometer Hybrid Diamond Nanosensors. *Science Advances* **2021**, *7* (3), eabd7888.
(13) Yanagi, T.; Kaminaga, K.; Kada, W.; Hanaizumi, O.; Igarashi, R. Optimization of Wide-Field ODMR Measurements Using Fluorescent Nanodiamonds to Improve Temperature Determination Accuracy. *Nanomaterials* **2020**, *10* (11), 2282.
(14) Maclaurin, D.; Hall, L. T.; Martin, A. M.; Hollenberg, L. C. L. Nanoscale Magnetometry through Quantum Control of Nitrogen–Vacancy Centres in Rotationally Diffusing Nanodiamonds. *New J. Phys.* **2013**, *15* (1), 013041.
(15) McGuinness, L. P.; Yan, Y.; Stacey, A.; Simpson, D. A.; Hall, L. T.; Maclaurin, D.; Prawer, S.; Mulvaney, P.; Wrachtrup, J.; Caruso, F.; Scholten, R. E.; Hollenberg, L. C. L. Quantum Measurement and Orientation Tracking of Fluorescent Nanodiamonds inside Living Cells. *Nat. Nanotechnol.* **2011**, *6* (6), 358–363.
(16) Igarashi, R.; Sugi, T.; Sotoma, S.; Genjo, T.; Kumiya, Y.; Walinda, E.; Ueno, H.; Ikeda, K.; Sumiya, H.; Tochio, H.; Yoshinari, Y.; Harada, Y.; Shirakawa, M. Tracking the 3D Rotational Dynamics in Nanoscopic Biological Systems. *J. Am. Chem. Soc.* **2020**, *142* (16), 7542–7554.
(17) Terada, D.; Sotoma, S.; Harada, Y.; Igarashi, R.; Shirakawa, M. One-Pot Synthesis of Highly Dispersible Fluorescent Nanodiamonds for Bioconjugation. *Bioconjugate Chem.* **2018**, *29* (8), 2786–2792.
(18) Lanin, A. A.; Fedotov, I. V.; Ermakova, Y. G.; Sidorov-Biryukov, D. A.; Fedotov, A. B.; Hemmer, P.; Belousov, V. V.; Zheltikov, A. M. Fiber-Optic Electron-Spin-Resonance Thermometry of Single Laser-Activated Neurons. *Opt. Lett.* **2016**, *41*, 5563.
(19) Barry, J. F.; Turner, M. J.; Schloss, J. M.; Glenn, D. R.; Song, Y.; Lukin, M. D.; Park, H.; Walsworth, R. L. Optical Magnetic Detection of Single-Neuron Action Potentials Using Quantum Defects in Diamond. *Proc. Natl. Acad. Sci. U. S. A.* **2016**, *113*, 14133.
(20) Barson, M. S. J.; Peddibhotla, P.; Ovartchaiyapong, P.; Ganesan, K.; Taylor, R. L.; Gebert, M.; Mielens, Z.; Koslowski, B.; Simpson, D. A.; McGuinness, L. P.; McCallum, J.; Prawer, S.; Onoda, S.; Ohshima, T.; Bleszynski Jayich, A. C.; Jelezko, F.; Manson, N. B.; Doherty, M. W. Nanomechanical Sensing Using Spins in Diamond. *Nano Lett.* **2017**, *17* (3), 1496–1503.
(21) Hsieh, S.; Bhattacharyya, P.; Zu, C.; Mittiga, T.; Smart, T. J.; Machado, F.; Kobrin, B.; Höhn, T. O.; Rui, N. Z.; Kamrani, M.; Chatterjee, S.; Choi, S.; Zaletel, M.; Struzhkin, V. V.; Moore, J. E.; Levitas, V. I.; Jeanloz, R.; Yao, N. Y. Imaging Stress and Magnetism at High Pressures Using a Nanoscale Quantum Sensor. *Science* **2019**, *366* (6471), 1349–1354.
(22) Dolde, F.; Fedder, H.; Doherty, M. W.; Nöbauer, T.; Rempp, F.; Balasubramanian, G.; Wolf, T.; Reinhard, F.; Hollenberg, L. C. L.; Jelezko, F.; Wrachtrup, J. Electric-Field Sensing Using Single Diamond Spins. *Nat. Phys.* **2011**, *7* (6), 459–463.
(23) Iwasaki, T.; Naruki, W.; Tahara, K.; Makino, T.; Kato, H.; Ogura, M.; Takeuchi, D.; Yamasaki, S.; Hatano, M. Direct Nanoscale Sensing of the Internal Electric Field in Operating Semiconductor Devices Using Single Electron Spins. *ACS Nano* **2017**, *11* (2), 1238–1245.
(24) Taylor, J. M.; Cappellaro, P.; Childress, L.; Jiang, L.; Budker, D.; Hemmer, P. R.; Yacoby, A.; Walsworth, R.; Lukin, M. D. High-Sensitivity Diamond Magnetometer with Nanoscale Resolution. *Nat. Phys.* **2008**, *4* (10), 810–816.
(25) Duan, D.; Kavatamane, V. K.; Arumugam, S. R.; Rahane, G.; Du, G.-X.; Tzeng, Y.-K.; Chang, H.-C.; Balasubramanian, G. Laser-Induced Heating in a High-Density Ensemble of Nitrogen-Vacancy Centers in Diamond and Its Effects on Quantum Sensing. *Opt. Lett.* **2019**, *44* (11), 2851.
(26) Wang, J.-F.; Cui, J.-M.; Yan, F.-F.; Li, Q.; Cheng, Z.-D.; Liu, Z.-H.; Lin, Z.-H.; Xu, J.-S.; Li, C.-F.; Guo, G.-C. Optimization of Power Broadening in Optically Detected Magnetic Resonance of Defect Spins in Silicon Carbide. *Phys. Rev. B: Condens. Matter Mater. Phys.* **2020**, *101* (6), 064102.
(27) Bogdanov, S.; Shalaginov, M. Y.; Akimov, A.; Lagutchev, A. S.; Kapitanova, P.; Liu, J.; Woods, D.; Ferrera, M.; Belov, P.; Irudayaraj, J.; Boltasseva, A.; Shalaev, V. M. Electron Spin Contrast of Purcell-Enhanced Nitrogen-Vacancy Ensembles in Nanodiamonds. *Phys. Rev. B: Condens. Matter Mater. Phys.* **2017**, *96* (3), 035146.
(28) Alegre, T. P. M.; Santori, C.; Medeiros-Ribeiro, G.; Beausoleil, R. G. Polarization-Selective Excitation of Nitrogen Vacancy Centers in Diamond. *Phys. Rev. B: Condens. Matter Mater. Phys.* **2007**, *76* (16), 165205.
(29) Fujisaku, T.; Tanabe, R.; Onoda, S.; Kubota, R.; Segawa, T. F.; So, F. T.-K.; Ohshima, T.; Hamachi, I.; Shirakawa, M.; Igarashi, R. PH Nanosensor Using Electronic Spins in Diamond. *ACS Nano* **2019**, *13* (10), 11726–11732.
(30) Zhang, D. A Coefficient of Determination for Generalized Linear Models. *Am. Stat.* **2017**, *71* (4), 310–316.
(31) Reineck, P.; Lau, D. W. M.; Wilson, E. R.; Fox, K.; Field, M. R.; Deeleepojananan, C.; Mochalin, V. N.; Gibson, B. C. Effect of Surface Chemistry on the Fluorescence of Detonation Nanodiamonds. *ACS Nano* **2017**, *11* (11), 10924–10934.

https://doi.org/10.1021/acsmeasuresciau.1c00009
ACS Meas. Au 2021, 1, 20–26